

Segmentation of Anatomical Layers and Artifacts in Intravascular Polarization Sensitive Optical Coherence Tomography Using Attending Physician and Boundary Cardinality Lost Terms

Mohammad Haft-Javaherian, Martin Villiger, Kenichiro Otsuka, Joost Daemen, Peter Libby, Polina Golland*, and Brett E. Bouma*

Abstract—Cardiovascular diseases are the leading cause of death and require a spectrum of diagnostic procedures as well as invasive interventions. Medical imaging is a vital part of the healthcare system, facilitating both diagnosis and guidance for intervention. Intravascular ultrasound and optical coherence tomography are widely available for characterizing coronary stenoses and provide critical vessel parameters to optimize percutaneous intervention. Intravascular polarization-sensitive optical coherence tomography (PS-OCT) can simultaneously provide high-resolution cross-sectional images of vascular structure while also revealing preponderant tissue components such as collagen and smooth muscle and thereby enhance plaque characterization. Automated interpretation of these features would facilitate the objective clinical investigation of the natural history and significance of coronary atherosclerosis. Here, we propose a convolutional neural network model and optimize its performance using a new multi-term loss function to classify the lumen, intima, and media layers in addition to the guidewire and plaque artifacts. Our multi-class classification model outperforms the state-of-the-art methods in detecting the anatomical layers based

on accuracy, Dice coefficient, and average boundary error. Furthermore, the proposed model segments two classes of major artifacts and detects the anatomical layers within the thickened vessel wall regions, which were excluded from analysis by other studies. The source code and the trained model are publicly available at <https://github.com/mhaft/OCTseg>.

Index Terms—Boundary Detection, Optical Coherence Tomography, Polarization Sensitive, Segmentation, Vessels

I. INTRODUCTION

CORONARY artery disease accounts for 365 thousand deaths per year and more than one million individuals suffered from acute coronary events last year in the United States [1]. Although effective therapies are available and several novel treatments are in development, predicting and preventing acute coronary events still presents a major challenge [2]. In addition to the physical examination and blood biomarkers, physicians diagnose coronary artery disease in symptomatic patients using various non-invasive imaging tests such as nuclear stress tests, CT coronary angiography, and PET-CT. Similarly, the guidance of percutaneous coronary interventions relies increasingly on invasive imaging modalities, which may offer a window of opportunity to prospectively identify lesions with a propensity for subsequent acute events. Since coronary atherosclerosis is the primary underlying cause of acute myocardial infarction, the adoption of sensitive tools for vessel and plaque characterization is essential [3]. To guide angioplasty and stenting, detecting the structure and composition of plaques is essential to select stent optimal diameter, length, and landing zone [4]. Important plaque features include the location and extent of atheromatous lipid pools, the location and shape of calcifications, the lumen area, and reference vessel diameter [5].

Intravascular (IV) optical coherence tomography (OCT) acquires the highest resolution images of the subsurface microstructure of coronary atherosclerotic lesions available in catheterization laboratories [6], [7]. The high-resolution IV-OCT images enable the development and application of new therapeutic procedures to improve clinical outcomes [4], [8].

This work was supported by the National Institutes of Health NIBIB under Grants P41EB-015902 and P41EB-015903. Also, Mohammad Haft-Javaherian was supported by Bullock Postdoctoral Fellowship. This work was done partially using MIT-IBM Satori hardware resource (Corresponding author:).

* Polina Golland and Brett E. Bouma have equal contributions.

Mohammad Haft-Javaherian is with the Wellman Center for Photomedicine, Massachusetts General Hospital, Harvard Medical School, Boston, MA 02114 USA, and the Computer Science and Artificial Intelligence Laboratory (CSAIL), Massachusetts Institute of Technology, Cambridge, MA 02142 USA (e-mail: haft@csail.mit.edu).

Martin Villiger and Kenichiro Otsuka are with the Wellman Center for Photomedicine, Massachusetts General Hospital, Harvard Medical School, Boston, MA 02114 USA (e-mail: mwilliger@mgh.harvard.edu; kotsuka@mgh.harvard.edu).

Joost Daemen is with the Department of Interventional Cardiology, Thoraxcenter, Erasmus Medical Center, Rotterdam, The Netherlands (e-mail: j.daemen@erasmusmc.nl).

Peter Libby is with the Division of Cardiovascular Medicine, Department of Medicine, Brigham and Women's Hospital, Harvard Medical School, Boston, MA 02115 (e-mail: plibby@bwh.harvard.edu).

Polina Golland is with the Computer Science and Artificial Intelligence Laboratory (CSAIL), Massachusetts Institute of Technology, Cambridge, MA 02142 USA (e-mail: polina@csail.mit.edu).

Brett E. Bouma is with the Wellman Center for Photomedicine, Massachusetts General Hospital, Harvard Medical School, Boston, MA 02114 USA, and the Institute for Medical Engineering and Science, Massachusetts Institute of Technology, Cambridge, MA 02142 USA (e-mail: bouma@mgh.harvard.edu).

Nonetheless, the interpretation and characterization of OCT images require extensive training and experience due to the image contrast, signal statistics, and speckle characteristics. These difficulties result in modest intra- and inter-reader agreement and limit more widespread adoption of OCT [9]. Furthermore, the image processing algorithms used in the clinical setting are currently limited to the lumen segmentation task without extracting the remaining embedded information in the images. Notably, the automatic detection of the anatomical layers within the vessel wall and other features beyond the lumen would accelerate the OCT utilization in clinical settings and translational research by eliminating the need for extensive training and time-consuming manual segmentation.

In parallel to conventional OCT, polarization sensitive (PS) OCT performs polarimetry to retrieve tissue birefringence and depolarization images. Nadkarni et al. [10] demonstrated that fibrillar tissues such as interstitial collagen and arterial smooth muscle cell arrays are birefringent. Villiger, et al, showed that tissues containing lipid particles, macrophage accumulations, or cholesterol crystals exhibit depolarization [11]. Intimal thickness is an important early clinical sign of atherosclerosis [12] and can be measured by detecting the outer boundary of the intima (i.e., the internal elastic lamina (IEL)) based on the birefringence difference between intima and media layers. Moreover, Villiger et al. [11] characterized human coronary atherosclerosis by utilizing the PS-OCT signatures and showed their correlation with the histological features. Therefore, the supplementary multi-dimensional PS-OCT signals facilitate the downstream image analyses and enhance the automatic and objective tissue characterizations.

Current computer vision and machine learning advancements are transforming medicine, particularly imaging modalities in different specialties such as radiology and cardiology [13], [14]. Specifically, deep learning (DL) algorithms such as convolutional neural networks (CNN) trained in supervised settings demonstrate superior performance when the ground-truth manual data is attainable and generalizable [15]. In different circumstances, different training strategies such as unsupervised, weakly-supervised, or transfer learning can be adopted successfully [16], [17]. The strong capabilities of these modern computer vision models benefit, in particular, the problems that involve complex multi-dimensional data and require time-consuming and expensive manual analyses.

This paper proposes a convolutional neural network and optimizes its performance using a new multi-term loss function to utilize the advantage of the PS-OCT imaging modality and analyze the coronary artery images automatically. The proposed model detects the vessel lumen, two anatomical layers, and two types of prominent artifacts. Our work improves the boundary detection of lumen and anatomical layers while adding the ability to detect the artifacts and handle the cases excluded by other studies. The application of automatic coronary artery image analysis could ultimately improve patient care outcomes and cost-effectiveness [18].

II. RELATED WORK

The clear need for automated segmentation and interpretation of intravascular OCT images has motivated the develop-

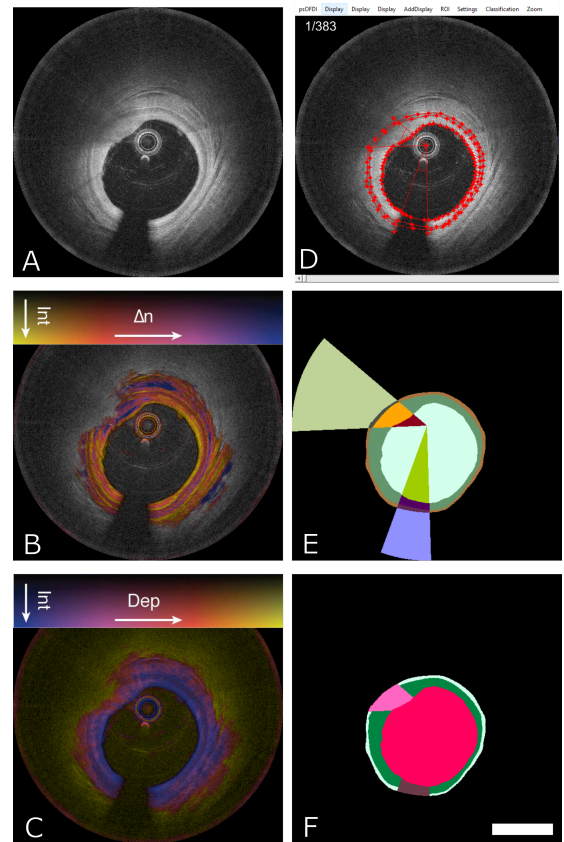


Fig. 1. The expert annotation of IV PS-OCT images. An example of multi-channel IV PS-OCT cross-section image including backscatter signal intensity (A), birefringence (B), and depolarization (C) channels. D, the manual annotation by an expert using our Matlab graphical user interface. E, Inclusive pixel-level labels using the manual annotation encoded by the pixel intensity's integer bits. F, Equivalent exclusive labels defined in Table I. Scale bar: 2 mm.

ment of a range of methods that offer different approaches to tackling the various challenges and artifacts presented by typical intravascular OCT data sets.

OCT axial (A) lines are independently acquired along the radial direction of the vessel in cylindrical coordinates owing to the probe rotation. Simultaneous pullback of the probe along the vessel results in a helical scan pattern. Contemporary IV-OCT reconstructs individual A-lines from measurements in the spectral domain and displays the logarithm of the power of the reconstructed signal in dB scale. Researchers proposed various digital signal processing techniques to analyze A-lines in order to exploit the complex characteristics of the OCT signal [19]–[23].

Ughi et al. [24] detected the vessel lumen by utilizing the prior cross-sectional information, including the lumen boundary signal signatures and topological relationships between visible objects in each A-line. Their algorithm performed well on two evaluated datasets, yet it relies on manually optimized parameters that likely require adjusting when applied to different datasets. In the same manner, Joseph et al. [25] used the transmissivity map, i.e., the inverse of the attenuation coefficient, to enhance the lumen contrast before local region-based active contour segmentation with a level-set energy function. The energy function has image-dependent and

length-penalizing regularization terms and utilizes the local speckle statistics. Remaining artifacts were corrected using dynamic programming. Similarly, Cao *et al.* [26] used a gradient-based distance-regularized level-set followed by divide-and-conquer-based post-processing to stabilize the segmentation. However, level-set methods perform poorly in low signal-to-noise (SNR) regions and result in non-smooth and imprecise lumen boundaries.

Graphical models such as graph-cuts are suitable solutions for this problem because the lumen boundary and the interfaces of anatomical layers are not intersecting. Graphical methods reformulate the image segmentation as common optimization and common graph problems by mapping the pixels and their relationships into a multi-dimensional geometrical graph [27]. For instance, the graph-cut method minimizes the graph energy based on the max-flow min-cut theorem to obtain an optimal set of graph nodes representing the target segmentation. Zahnd *et al.* [28] preprocessed IV-OCT images by removing A-lines containing artifacts and constructed a continuous data-driven graph representation with an additional dimension to represent the multi-layered wall structure. Subsequently, they adopted image gradient and smoothness terms to generate a parametric energy function over the last dimension to constrain the optimization within the radial direction. Lee *et al.* [29] considered smoothness terms along both axes for each anatomical layer to enforce 3D surface smoothness while attracting the layer boundaries toward the gradient field's extrema in a multi-step fashion. Chen *et al.* [30] improved the plausibility of the segmentation results by considering the thickness range of anatomical layers as prior knowledge.

In distinction to energy functions based on the image intensity gradient, Roy *et al.* [31] proposed an physics-based energy term, *i.e.*, optical backscattering, and used the graphical model's output as the seed point for the following random walk method. While other graphical models such as Markov random field [32] tackle the vessel wall segmentation problem from a similar point of view, the counterpart physics-based methods simulate the segmentation as a physical problem. For example, Olender *et al.* [33] proposed a model based on mechanical deformation that mimics active contour models [34].

Albeit graphical methods demonstrated success in solving the problem at hand, difficulties arise in low SNR regions with speckles, anatomical anomalies, and external objects, which limits the practicality of these models and causes a cascade of increasing errors that require follow-up manual corrections done by expert annotators at the post-processing stage [35].

In recent years, the new machine learning models are emerging solutions to many medical image analysis problems. Yong *et al.* [36] represented the vessel wall layers similar to the graphical models and used a regression deep learning (DL) network to detect the vessel lumen along the radial direction directly in polar coordinates. Gharaibeh *et al.* [37] segmented vessel lumen and coronary calcifications in IV-OCT images using a U-Net architecture and post-processed the output with a conditional random field model. Abdolmanafi *et al.* [16], [17] used pre-trained convolutional neural networks (CNN) to segment the anatomical layers of the coronary arteries using transfer learning. Our model is based upon these

previous studies' findings and extends on the-state-of-the-art DL methods to improve its performance and capability.

III. METHODS

A. Study group

This work is a retrospective analysis of an intravascular polarimetry pilot study, which included two cohorts and enrolled a total of 57 (30+27) patients who underwent percutaneous coronary intervention and PS-OCT imaging from December 2014 to July 2015 (cohort 1) and from June 2018 to January 2019 (cohort 2) at the Erasmus University Medical Center in Rotterdam. All included PS-OCT pullbacks are acquired in the coronary artery before the procedure.

The Ethics Committee of Erasmus University Medical Center approved the study protocol, and all patients gave written informed consent. All procedures were performed in accordance with local and federal regulations and the Declaration of Helsinki.

B. Imaging

The imaging system consists of "FastView" intravascular catheters (Terumo Co., Tokyo, Japan) interfaced with our custom-built PS-OCT system, operating at 1300 nm central wavelength similar to commercially available clinical IV-OCT systems. The wavelength scanning range was 110 nm, achieving a radial resolution below 10 μm , assuming a tissue refractive index of 1.34. The dimension of the pixels in the reconstructed tomograms in the radial direction were 4.2 μm and 4.43 μm , respectively, for the two cohorts. The catheter's rotation speed was 100 RPS, with 1024 radial scans per rotation, and pullbacks were performed at 20 mm/s or 40 mm/s, at the operator's discretion. Non-ionic contrast solution was injected at a rate of 3-4 mL/s during the pullback to displace coronary blood and obtain an unperturbed view of the vessel wall.

C. Polarimetry

Intravascular polarimetry was performed based on our earlier work [11], [38]–[40]. Briefly, an electro-optic polarization modulator was used to alternate the polarization state of the light incident on the tissue between consecutive depth scans and a polarization-diverse receiver enabled determination of the detected light's polarization state and intensity. Polarimetric analysis employed spectral binning [41] to reconstruct maps of tissue birefringence and depolarization.

Birefringence is the difference in the refractive index experienced by orthogonal polarization states aligned and orthogonal to the tissue optic axis, respectively. Tissue depolarization measures the randomness of the detected light's polarization state using the complement to one of the degree of polarization.

D. Manual annotations

Initially, an expert interventional cardiologist (KO) excluded partial segments of 3D pullbacks that suffered from artifacts caused by insufficient blood clearing. The qualified pullback

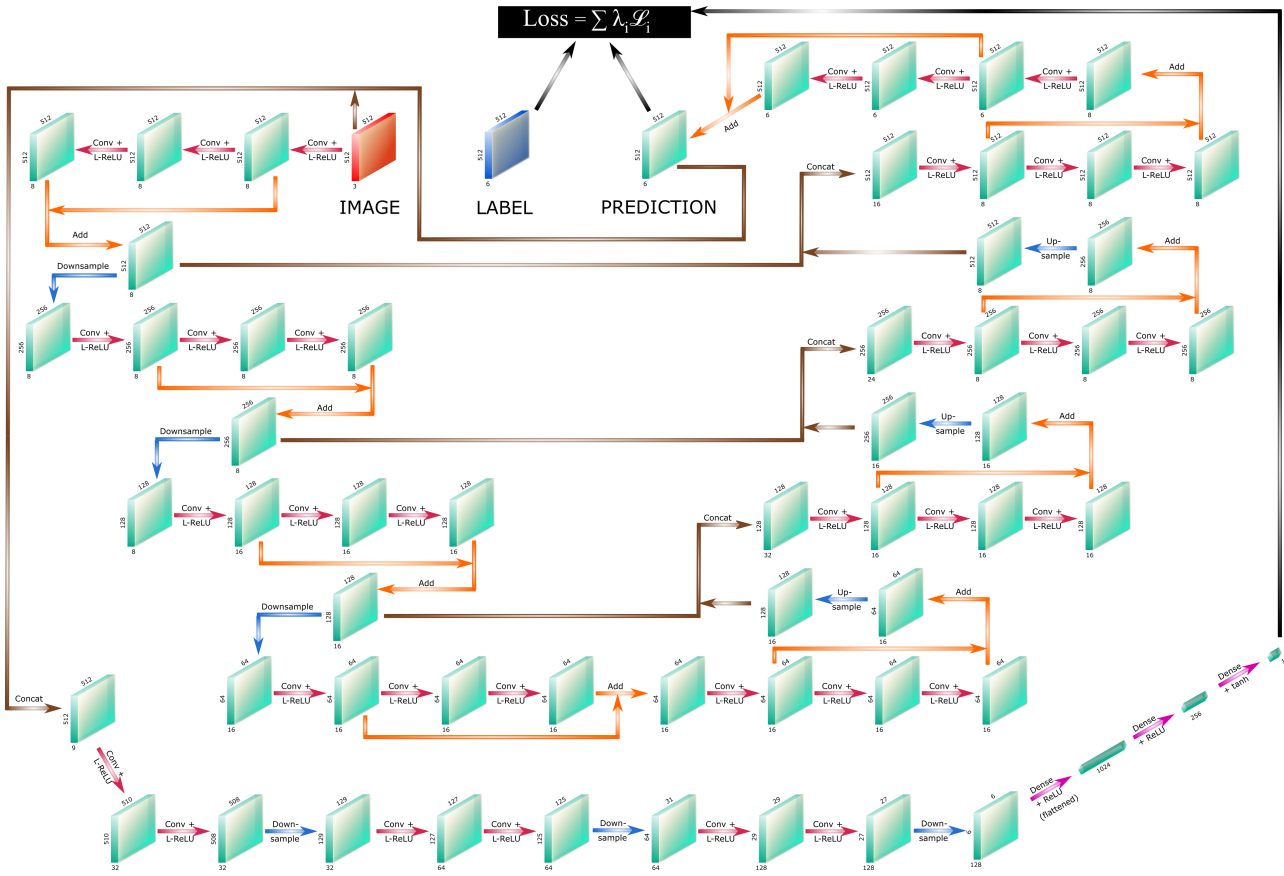


Fig. 2. The proposed model architecture. The main model has a multi-channel image as the input and a multi-class probability prediction as the output. The auxiliary critique model (a.k.a. Attending Physician) concatenates the image and ground-truth label as its input to predict the quality level of manual labeling. After training, this model was used as one of the loss terms.

segments added up to 3936 mm of pullbacks at a 100 or 200 μm pitch. Subsequently, the expert annotated a total of 984 cross-sections spaced 4 mm apart using our home built Matlab graphical user interface. The manual annotations included the outer boundaries of the lumen, tunica intima (i.e., internal elastic lamina (IEL)), and tunica media (i.e., external elastic lamina (EEL)). The location of IEL and EEL within the plaque and guidewire shadows are extrapolated based on their visible segments. Additionally, A-lines containing plaque, guidewires, stent struts, side branches, or thrombus were identified and used for segmentation or selective analysis without influencing the main label categories. Consequently, as summarized in Table I, the manual annotations were converted into six exclusive labels: background, lumen, visible intima, visible media, plaque shadow, and guidewire shadow.

To manage the workload, we annotated the total dataset in four separate batches and through three phases: initial annotation, high-precision annotation, and annotation approval. One of the batches was revised extensively at the pixel-level, requiring four-fold longer annotation time. The high-accuracy batch, in combination with its initial annotation, was utilized to train the proposed critique model and its resulting loss term.

E. CNN architecture

The proposed network architecture scheme is based on the U-Net [42] and deep residual learning [43] models. The op-

TABLE I

THE DEFINITION OF THE SIX EXCLUSIVE LABELS THAT ARE BASED ON THE MANUAL EXPERT ANNOTATIONS AND SHOWN IN FIG. 1.D.

Class	Label	Definition
1	Outside	external elastic lamina and deeper tissues
2	Lumen	Interior of the convex vessel lumen
3	Intima	visible tunica intima
4	Media	visible tunica media
5	G-Shadow	guidewire shadows between lumen and EEL
6	P-Shadow	plaque shadows between lumen and EEL

timized architecture contains multi-scale encoder and decoder sections with skip connections at each scale. The convolutional complex contains three convolutional layers with a 3×3 pixel kernel size and a leaky version of the rectified linear unit (L-ReLU) activation function, which has a negative slope coefficient of 0.3. These three convolutional layers calculate the residual values by using an internal skip connection. The max-pooling layers with a 2×2 pixel kernel size are applied after convolutional complexes in the encoding section for down-scaling while the counterpart deconvolutional layers are applied for bi-linear up-scaling within the decoding section. The encoding output and decoding input are connected through two convolutional complexes that operate at the latent repre-

sensation level. The layers within each of the three scales and the latent representation layers have 8, 8, 16, and 16 features, respectively.

The critique model architecture accepts the concatenation of image channels and output label channels as the input and applies three convolutional complexes with 32, 64, and 128 features, respectively. Each complex consists of two convolutional layers with a 3×3 pixel kernel size and the ReLU activation function followed by a max-pooling with a 2×2 pixel kernel size. The last complex's output is flattened and fed into a three-layer dense neural network with 1024, 256, and 128 hidden nodes and ReLU activation function. The final output has one feature and uses the hyperbolic tangent activation function.

F. Loss function

We developed a multi-term multivariate loss function that includes novel loss terms. The first loss term is the weighted cross-entropy function,

$$\mathcal{L}_{WCE}(\mathbf{y}, \hat{\mathbf{y}}) = -\frac{1}{N} \sum_{c=1}^{N_c} \omega_c \sum_{i,j} [\mathbf{y}_{ijc} \log \hat{\mathbf{y}}_{ijc}], \quad (1)$$

that measures the cross-entropy between the target label (y) and predicted label probabilities (\hat{y}) of all N pixels where i and j are 2D matrix indices and c is the class index. Each pixel's cross-entropy is then weighted proportionately to the inverse of its class population (ω_c).

The second loss term is a multi-class version of the generalized Dice loss function [44],

$$\mathcal{L}_{Dice}(\mathbf{y}, \hat{\mathbf{y}}) = 1 - \frac{2}{N_c} \sum_{c=1}^{N_c} \frac{\sum_{i,j} [\mathbf{y}_{ijc} \times \hat{\mathbf{y}}_{ijc}] + \epsilon}{\sum_{i,j} [\mathbf{y}_{ijc}^2 + \hat{\mathbf{y}}_{ijc}^2] + \epsilon}, \quad (2)$$

which measures each label's segmentation accuracy similar to the Dice coefficient. Dice loss uses the prediction probability (e.g. softmax of logits) instead of the classification result and ranges from zero to one, with zero corresponding to the most accurate result. In comparison to the Dice coefficient, the argument of the maxima is omitted in order to make the function differentiable, and we added a small number (ϵ) for numerical stability.

The weighted cross-entropy and Dice loss terms are only marginally affected by the boundary inaccuracies noticeably because the boundary pixels are a small portion of the target objects. Nevertheless, the quality of the label is notably affected by the boundary precision. For this reason, the third loss term is based on the boundary precision and focuses the network's attention on the close vicinity of label boundaries. The boundary precision loss term (\mathcal{L}_{BP}) utilizes a boundary neighborhood mask,

$$\beta(\mathbf{y}) = \left(\bigvee_{c=1}^{N_c} [(\mathbf{1}_{b \times 1} * \mathbf{y}_k) \oplus (\mathbf{y}_k)] \right) \bigvee \left(\bigvee_{c=1}^{N_c} [(\mathbf{1}_{b \times 1} * (1 - \mathbf{y}_k)) \oplus (1 - \mathbf{y}_k)] \right), \quad (3)$$

which masks the cross-entropy loss values of the pixels that are not in close vicinity of the label boundaries along the radial axis (e.g. $\leq b$, $b = 10$ pixels). The boundary precision loss term,

$$\mathcal{L}_{BP}(\mathbf{y}, \hat{\mathbf{y}}, \beta) = \frac{-1}{\sum_{i,j} \beta_{ij}} \sum_{c=1}^{N_c} \sum_{i,j} \beta_{ij} \mathbf{y}_{ijc} \log \hat{\mathbf{y}}_{ijc}, \quad (4)$$

is differentiable with respect to the model parameters as long as β is a function of the ground-truth target label.

As mentioned in the description of the manual annotation, one of the four dataset batches was revised extensively with pixel-level precision, which required four-fold longer annotation time. This practice resembles the scenario of an attending physician reviewing and scoring manual annotations done by resident physicians to provide constructive feedback for training. Analogously, we trained a model to critique the multi-class labels conditioned on their input images by distinguishing between the first and final revision of the labels within the $[-1, +1]$ range, respectively. After training, the critique mode The critique model learns a probability distribution of the first and final revisions defined on the image and label and located in a very high-dimensional probability density domain. The trained model was used the attending physician loss term (\mathcal{L}_{AP}) to critique the quality of predicted labels. The training of a critique model involves a loss function that measures the distance of model parameters to the optimal solution in the parameter space. Arjovsky et al. [45] proposed *Wasserstein-1* (a.k.a. Earth-Mover) distance,

$$W_1(P, P') = \inf_{\gamma \in \Pi(P, P')} \mathbb{E}_{(x, x') \sim \gamma} \|x - x'\|^1, \quad (5)$$

where $\Pi(P, P')$ is the set of all joint distributions $\gamma(x, x')$ that their marginal distributions are equal to P and P' . *Wasserstein-1* is the optimal cost of transporting a mass with distribution P to another mass with distribution P' when the transport cost and transport distance are linearly related. Stable learning with a meaningful learning curve that avoids common problems including mode collapse can be obtained when *Wasserstein-1* distance is adopted [45]. Since the infimum in 5 is intractable, Kantorovich and Rubinstein [46] proposed a tractable dual problem,

$$W_1(P, P') = \sup_{\|f\|_L \leq 1} \{\mathbb{E}_{x \sim P}[f(x)] - \mathbb{E}_{x' \sim P'}[f(x')]\}, \quad (6)$$

where f is a 1-Lipschitz function, mapping the support of P and P' to real numbers.

Similarly, we can select f from a family of parameterized functions ($\{f_w\}_{w \in \mathcal{W}}$) that are 1-Lipschitz or at least K -Lipschitz for a constant K and optimize Eq. 5 over the functional parameter space,

$$W_1(P, P') = \max_{w \in \mathcal{W}} \{\mathbb{E}_{x \sim P}[f_w(x)] - \mathbb{E}_{x' \sim P'}[f_w(x')]\}, \quad (7)$$

$$\nabla_w W_1(P, P') = \max_{w \in \mathcal{W}} \{\mathbb{E}_{x \sim P}[\nabla_w f_w(x)] - \mathbb{E}_{x' \sim P'}[\nabla_w f_w(x')]\}. \quad (8)$$

The requirement of f being K -Lipschitz for the function family of deep neural networks can be imposed by clipping

the parameter values with an absolute value upper limit [45] or enforcing the gradient of parameters to be 1 almost everywhere through a gradient penalty loss term [47]. Gulrajani et al. [47] showed that the gradient constraining method improves the learning process compared to the weight clipping method. We observed a similar effect while training our Attending Physician model, which is then used as the fourth loss term (\mathcal{L}_{AP}).

The last loss term examines the labels from a topological point of view. Ideally, the predicted labels along A-lines are composed of three or four connected components without any void, starting with the lumen label in the center and ending with the outside label. The area between the lumen and outside labels should be occupied by two adjacent solid anatomical layers (i.e., intima and media) or by one of the artifact labels (i.e., guidewire or plaque shadows). These configurations are distinguishable in terms of the number of label boundaries along the radial direction. The soft boundary cardinality loss term (\mathcal{L}_{BC}) penalize the discrepancy between the predicted and ground-truth labels based on the number of boundaries along the radial axis. We propose “soft argmax”,

$$\mathbf{S}(\mathbf{y}) = 1 + \tanh \left(M \left[\mathbf{y} - \max_c \mathbf{y}_{ijc} \right] \right), \quad (9)$$

which is a differentiable proxy for the arguments of the maxima and a saturated equivalent of the softmax function, i.e., $e^x / \|e^{x_i}\|_1$. The soft argmax admits the predicted class probabilities at each pixel and maps the probability of the most probable class and other classes to ~ 1 and ~ 0 , respectively. The level of saturation is controlled by the large number M and the precision of the probability values. Since the value of the soft argmax for a given class changes between two adjacent pixels at the label boundary, the soft boundary set cardinality along the radial axis,

$$\mathbf{BC}(\mathbf{S}) = \frac{1}{2} \sum_i \sum_c |\mathbf{S}(\mathbf{y})_{(i+1)jc} - \mathbf{S}(\mathbf{y})_{ijc}|, \quad (10)$$

approximates the number of class boundaries in each A-line. The boundary cardinality loss function (\mathcal{L}_{BC}),

$$\mathcal{L}_{BC}(\mathbf{y}, \hat{\mathbf{y}}) = \sigma(\mathbf{BC}(\mathbf{S}(\mathbf{y})), \mathbf{BC}(\mathbf{S}(\hat{\mathbf{y}}))), \quad (11)$$

compares the prediction and ground-truth labels with respect to the number of boundaries, where σ measures the difference between two \mathbf{BC} vectors (e.g. norm 1). We considered 1, 100, and $100/\epsilon$ for M , where ϵ is the small number used for mathematical stability in 2 and softmax value clipping. For σ , we considered $\|\cdot\|_1$, $\|\cdot\|_2$, and $\max(\cdot)$. Based on the validation dataset and the convexity of \mathcal{L}_{BC} , norm-1 ($\|\cdot\|_1$) and $100/\epsilon$ are the optimal choices for σ and M , respectively.

The final loss function combines all five loss terms,

$$\mathcal{L} = \lambda_{WCE} \mathcal{L}_{WCE} + \lambda_{Dice} \mathcal{L}_{Dice} + \lambda_{BP} \mathcal{L}_{BP} + \lambda_{AP} \mathcal{L}_{AP} + \lambda_{BC} \mathcal{L}_{BC}, \quad (12)$$

in which loss term weights (λ) are selected within the range $[10^{-3}, 10^3]$ and optimized over their logarithmically-spaced multidimensional grid using greedy algorithms.

G. Training and implementation

We randomly divided the final annotated dataset between training, validation, and hold-out testing dataset by selecting 45, 6, and 6 patients (80%/10%/10%), respectively. We augmented cross-sectional images with various transformations such as random mirroring or rotation, image intensity distribution manipulations, and spatial scaling to increase the model robustness and generalization. An element from the power set of the image augmentation set was applied to each given PS-OCT cross-section with randomly selected transformation parameters based on independent and identically uniformly distributed augmentation probabilities. The geometrical transformations were defined in the Cartesian coordinate system, but they were implemented and applied in the polar coordinate system. Finally, the data augmentation methods were implemented and executed on GPU to improve the model’s run-time.

We implemented our model in Python using Keras[™] and Tensorflow[™]. We commonly used RMSprop optimizer with $10^{-3} - 10^{-4}$ learning rate and mini-batch size of 20 per GPU. The GPU memory size was the limiting factor in the learning rate and mini-batch size selection. We used two NVIDIA[®] GeForce[®] RTX 2080 Ti or four NVIDIA[®] Tesla[®] V100.

H. Post-processing

We applied a post-processing procedure to the model output to enforce prior topological knowledge. Initially, small objects and holes within each class were removed, and their interfaces were smoothed. Then, a set of logical operations was applied to impose the topological relationships between the classes in the polar coordinate system. The proposed set includes the following operations:

- Lumen is a single connected object without any 2D void. The same rule applies to both guidewire shadow and outside.
- Guidewire and plaque shadows are confined between the lumen, the outside, and two A-lines.
- The order of layers from proximal to distal ends is lumen, intima, media, and outside.

I. Performance metrics

Performance metrics are essential for model comparisons, hyper-parameter tuning, and optimization monitoring during model training. Based on the ground-truth labels, we evaluated the performance of multi-class prediction models using accuracy and Dice coefficient,

$$Accuracy(\mathbf{Y}, \hat{\mathbf{Y}}) = \frac{1}{\|\mathcal{C}\|} \sum_{c \in \mathcal{C}} \frac{\|\mathbf{Y}\| - \|\mathbf{Y}_c \Delta \hat{\mathbf{Y}}_c\|}{\|\mathbf{Y}\|}, \quad (13)$$

$$Dice(\mathbf{Y}, \hat{\mathbf{Y}}) = \frac{2}{\|\mathcal{C}\|} \sum_{c \in \mathcal{C}} \frac{\|\mathbf{Y}_c \cap \hat{\mathbf{Y}}_c\|}{\|\mathbf{Y}_c\| + \|\hat{\mathbf{Y}}_c\|}, \quad (14)$$

where $\|\cdot\|$ is the set cardinality, $\hat{\mathbf{Y}}_c$ is the set of predicted pixels as class c , \mathbf{Y}_c is the set of pixels in ground-truth as class c , and \mathcal{C} is the set of classes. Furthermore, we evaluated the precision of inter-class boundaries using the average distance

TABLE II
LOSS TERMS ABLATION STUDY.

\mathcal{L}_{WCE}	\mathcal{L}_{Dice}	\mathcal{L}_{BP}	\mathcal{L}_{AP}	\mathcal{L}_{BC}	Accuracy	Dice	MHD
✓	×	×	×	×	94.6%	83.8%	7.2
✓	✓	×	×	×	94.3%	84.7%	6.0
✓	✓	✓	×	×	96.1%	88.3%	3.8
✓	✓	✓	✓	×	95.3%	86.5%	3.2
✓	✓	✓	✓	✓	96.0%	88.3%	2.3

error (ADE) along the radial direction and modified Hausdorff distance (MHD) [48] in 2D within the cross-section,

$$d(a, \mathcal{B}) = \inf_{b \in \mathcal{B}} \{\|a - b\|_2\}, \quad (15)$$

$$ADE(\hat{\mathcal{B}}; \mathcal{B}) = \frac{1}{\|\hat{\mathcal{B}}\|} \sum_{a \in \hat{\mathcal{B}}} d(a, \mathcal{B}), \quad (16)$$

$$MHD(\hat{\mathcal{B}}, \mathcal{B}) = \max\{ADE(\hat{\mathcal{B}}; \mathcal{B}), ADE(\mathcal{B}; \hat{\mathcal{B}})\}, \quad (17)$$

where \mathcal{B} and $\hat{\mathcal{B}}$ are the set of boundary pixels in the ground-truth and prediction, respectively, and $\|\cdot\|_2$ is the Euclidean norm.

IV. RESULTS

We developed and optimized a convolutional neural network model based on U-Net [42] and deep residual learning [43] architectures in addition to a new multi-term loss function to analyze PS-OCT images of the coronary arteries and detect the vessel lumen, two anatomical layers, and two types of prominent artifacts. The models were trained using the training dataset, while optimization of the model architecture and loss functions was based on the model's performance on the validation dataset. Ultimately, we evaluated the developed models using the hold-out test dataset.

We examined the advantage of using PS-OCT to visualize and disseminate anatomical layers compared to the conventional IV-OCT in a controlled experiment in confirmation with the evidence provided by our previous studies [11], [49]. The optimized architecture with the weighted cross-entropy loss function was trained using IV-OCT and PS-OCT, one at a time. The average Dice coefficient of two vessel wall classes for the models trained on the conventional IV-OCT and PS-OCT were 74.8% and 78.9%, respectively. The performance improvement confirms that the PS-OCT provides auxiliary information and facilitates the detection of anatomical layers.

Correspondingly, we conducted an ablation study to examine the individual effects of the proposed loss terms, i.e.,

- 1) The weighted cross-entropy loss term (\mathcal{L}_{WCE}),
- 2) The generalized soft multi-class dice loss term (\mathcal{L}_{Dice}),
- 3) The boundary precision loss term (\mathcal{L}_{BP}),
- 4) The Attending Physician (a.k.a. Wasserstein critique model) loss term (\mathcal{L}_{AP}), and
- 5) The soft boundary cardinality loss term (\mathcal{L}_{BC}).

We measured the accuracy, Dice coefficient, and modified Hausdorff distance (MHD) on the hold-out test dataset. Loss

TABLE III
COMPARISON OF OUR MODEL AND OTHER STUDIES THAT SEGMENT THE VESSEL LUMEN.

Model	Dice Coefficient	Other Metrics
Ughi et al. [24], [26]	96.9%	-
Joseph et al. [25]	78%	-
Cao et al. [26]	98.1%	-
Tung et al. [50]	97%	-
Wang et al. [51]	97%	-
Cheimariotis et al. [52]	93.5%	-
Moraes et al. [19]	97.1%	-
Bologna et al. [20]	-	TPR=97.4% TNR=99.5%
Macedo et al. [21]	97.5%	-
Tsantis et al. [32]	96.7%	-
Yong et al. [36]	98.5%	-
Macedo et al. [22]	97.0%	-
Olender et al. [33]	95.9%	-
Chen et al. [30]	-	ADE=2.37 μm
Yang et al. [34]	97.6%	-
Akbar et al. [23]	-	TPR=93.1%
Abdolmanafi et al. [17]	-	Acc=96%
Gharaibeh et al. [37]	98%	Acc=98%
Olender et al. [53]	-	Acc=94.9%
This Study	99.7%	ADE=2.36 μm Acc=99.8% TPR=99.7% TNR=99.9%

terms are appended in the order of their development and added by adopting the weights that were optimized based on greedy algorithms and follow-up fine-tuning perturbations.

The implementation and optimization of loss functions were devised and supervised by monitoring the Dice coefficient due to the unbalanced class populations, except for \mathcal{L}_{BC} that we additionally monitored by the boundary error based on MHD. The results of the ablation study on the loss terms are tabulated in Table II and affirm the effectiveness of all the loss terms and justify their inclusion.

For comparison with previous segmentation efforts, we compiled the reported performance of all previous studies, to the best of our knowledge, that developed segmentation methods for the lumen in Table III and for those that also segmented the two additional anatomical layers in Table IV.

Table III exhibits that our model outperforms other meth-

TABLE IV
COMPARISON OF OUR MODEL AND OTHER STUDIES THAT DETECT THE OUTER BOUNDARY OF LUMEN, INTIMA, AND MEDIA.

Study	Absolute Distance Error (μm)		
	Outer Lumen	Outer Intima	Outer Media
Zahnd et al. [28]	-	29 \pm 46	30 \pm 50
Chen et al. [30]	2.37 \pm 1.84	13.61 \pm 27.22	16.43 \pm 30.32
This Study	2.36 \pm 3.88	6.89 \pm 9.99	7.53 \pm 8.64

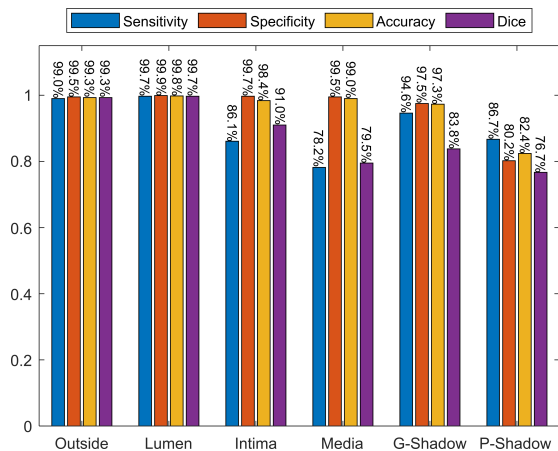


Fig. 3. The performance of our multi-label classification model based on different performance metrics.

ods in terms of Dice coefficient, accuracy (Acc), sensitivity (TPR), specificity (TNR), and average distance error (ADE). Moreover, Table IV indicates that our model has comparable performance in the outer lumen detection task and demonstrates lower absolute distance error (ADE) for both outer intima and media boundaries compared to the two other reports accomplishing this task. In order to enable a direct comparison, we excluded thickened vessel walls from evaluation of the outer boundaries, as proposed by Chen et al. [30]. However, thickened vessel walls are very common, especially in the population of patients likely to undergo intravascular imaging. Importantly, our model is able to segment cross-sections with thickened vessel wall with comparable performance, as summarized in Table V.

V. DISCUSSION

PS-OCT complements the IV-OCT backscatter intensity signal by measuring the scattered light's polarization state and reconstructing tissue birefringence and depolarization signals. These polarimetric signals provide a more detailed characterization of the vessel wall and can help to differentiate tissue layers that have comparable scattering properties but distinct polarization features. PS-OCT enriches the visualization of anatomical layers and facilitates the downstream image processing tasks. The present study proposes a convolutional neural network model with a new multi-term loss function to segment vessel lumen, intima layer, and media layer, that can leverage the increased contrast available to PS-OCT. Furthermore, the model works on all plaque types and correctly segments the intima and media boundaries behind thickened vessel wall, for as long as the plaques is not opaque. Conversely, segments of lipid-rich or calcified plaques that impede detection of the outer anatomical layers are identified as plaque shadows. The model also segments guidewire shadows.

Our high-performance and comprehensive multi-class image segmentation model can support many downstream image analysis tasks. Automated and objective image segmentation can serve to compute anatomical metrics and enable the formulation of clinical research questions that are currently impractical to address due to the workload of manual segmentation.

Crucially, automated segmentation also enables evaluation of tissue polarization properties in distinct anatomical areas, which previously relied on tedious manual segmentation [11], [38], [39]. In a clinical setting, automated segmentation could provide a simplified view of the culprit vessel and complement the currently used lumen diameter with information on the location, extent, and polarimetry-informed composition of plaques. This information could refine and optimize stent sizing.

While the aggregate performance metrics summarized in Table II allowed us to perform model comparisons and optimizations, the itemized performance measurements enable a more thorough inspection of the model. We highlight possible improvement areas based on Fig. 3 by considering different characteristics of each label, such as the label population and ground-truth noise distribution. The high-performance segmentation of the lumen and outside classes is a confirmation that we reached the limit of the ability to segment these classes by training models using a single-reader ground-truth. On the other hand, the media and shadow classes suffer from higher inter- and intra-reader ground-truth variability because they are located in the areas where signal quality is decaying and have lower performance compared to other classes. Nonetheless, these classes are great targets for future work and possibly benefit from unsupervised methodologies and ground-truth annotations done by a panel of readers. Even though PS-OCT has been demonstrated with the modified console, the mirror-state processing proposed by Xiong et al. [54] potentially accelerates the dissemination of anatomical layers and plaque features.

We compared the model's automated annotation results to the expert's ground-truth annotations in Fig. 4 to qualitatively characterize our model, illustrate the model's strengths, and identify possible areas of improvement. Our model's annotations and the ground-truth are overlaid on the gray-scale intensity image in blue and red outlines, respectively.

The most common complication for boundary annotation, particularly for the outer intima and outer media, is the presence of thick plaques or calcium (e.g. Fig. 4.A green arrow) and thickened vessel walls (e.g. Fig. 4.G, green arrow) that cause significant reduction in the detected signal. The background signal and statistical noise characteristics within the plaque regions impede the model's objective to annotate the anatomical layers and result in higher annotation variability (e.g. Fig. 4.F, yellow arrow; Fig. 4.G, yellow arrow; Fig. 4.K, yellow arrow).

Nonetheless, whenever the image information supports the ground-truth boundaries, the model matches well with the expert annotations even in these challenging cases (e.g. Fig. 4.D, both arrows). Correspondingly, the boundaries detected by the model may conform with the underlying multi-dimensional images more accurately than the ground-truth annotations (e.g. Fig. 4.F, green arrow), suggesting inconsistencies in the manual ground-truth segmentation.

In like manner, the guidewire obstructs the probing light causing a fuzzy signal at its boundaries, resulting in imprecise automatic and manual boundary detection (e.g. Fig. 4.B, green arrow). Moreover, the physical proximity of the vessel lumen

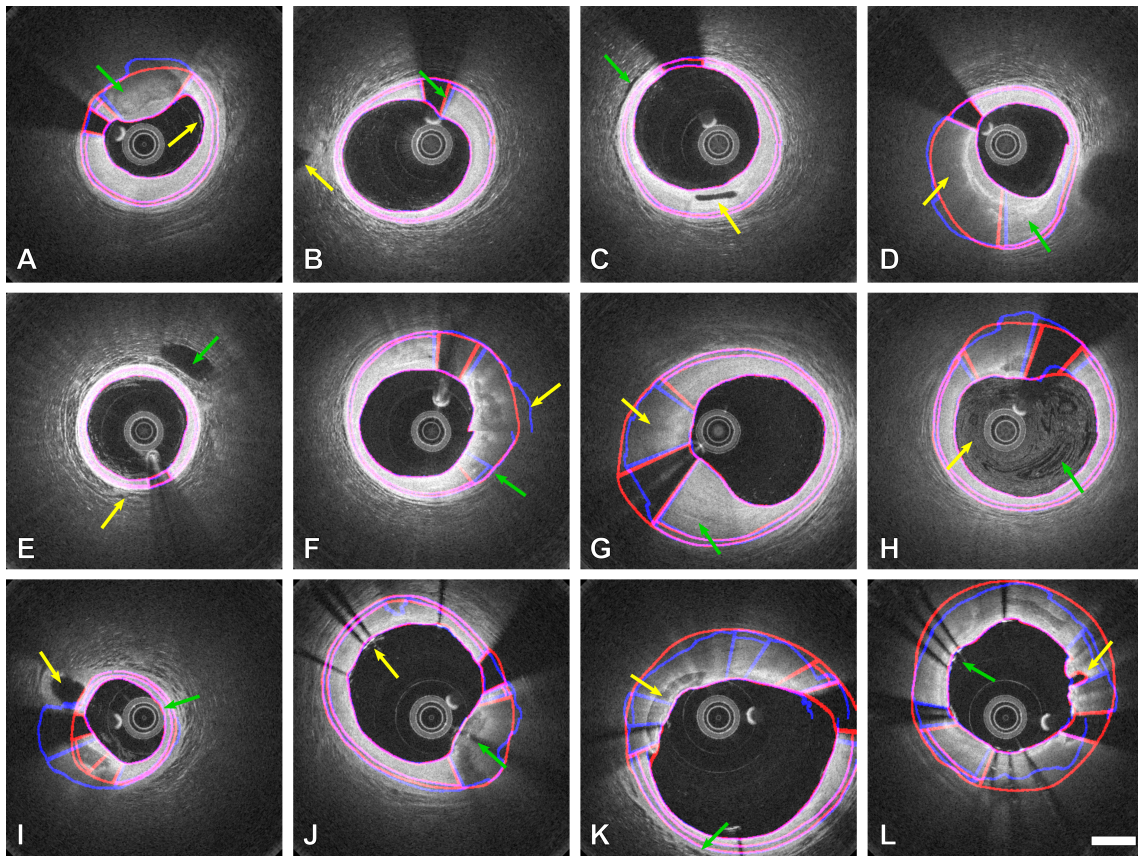


Fig. 4. Qualitative assessment of PS-OCT cross-sections. The annotations of our model and the ground-truth are overlaid on the gray-scale intensity image in blue and red outlines, respectively. See the text for detailed discussion. Scale bar: 1 mm.

with the guidewire and catheter leads to perturbed pixel-level delineation of the lumen boundary (e.g. Fig. 4.B, green arrow; Fig. 4.I, green arrow).

Side branches can appear in various locations of the field of view and could be expected to exhibit confusing features, yet our model analyzes these cases in concordance with the ground truth annotation. Such vessels might appear outside the vessel wall (e.g. Fig. 4.B, yellow arrow; Fig. 4.E, green arrow), directly adjacent to the vessel wall boundary (e.g. Fig. 4.I, yellow arrow), inside the intima (e.g. Fig. 4.C, yellow arrow), or in direct communication with the lumen (e.g. Fig. 4.L, yellow arrow).

Even though non-ionic contrast solution is injected during catheter pull-back to displace blood, residues of blood may persist in the vessel lumen vicinity (e.g. Fig. 4.A, yellow arrow; Fig. 4.E, yellow arrow). Blood clearance can be incomplete, especially at the onset or the end of contrast injection (Fig. 4.H, both arrows). Still, in all these cases, our model successfully detects the lumen outer boundaries. Equivalently, the dark and bright tissue patterns (e.g. Fig. 4.C, green arrow; and Fig. 4.K, green arrow) are observed beyond the media layer and mimic the multi-layer vessel wall structures but they do not distract the automatic boundary allocations.

Finally, while our study only included intravascular imaging prior to intervention, previously embedded stents are commonly encountered, owing to the high recurrence rate of acute coronary syndrome and myocardial infarction. Depending on

the specific stent material and patient history, stents might appear embedded in the vessel wall (e.g. Fig. 4.J, green arrow) or protruding into the lumen (e.g. Fig. 4.J, yellow arrow; Fig. 4.L, green arrow). Stents generate diverse and strong image artifacts that impede the model's ability to correctly detect the boundaries. Exact layer segmentation behind stents presents challenges even for expert readers. With the exception of neointimal hyperplasia, previously stented segments are unlikely to reside in the culprit segment. Such segments were included in our data set merely to train the model to ignore the ensuing artifacts. Notably, there exists a distinct class of models designed to detect stent struts and verify correct stent deployment [24], [32], [34]).

VI. CONCLUSION

This work presents a method to automatically and objectively segment the vessel lumen, intima layer, media layer, guidewire shadow, and plaque shadow in PS-OCT images. Our new and customized multi-term loss function and the PS-OCT auxiliary information appended to the conventional IV-OCT empower the model to detect anatomical layers of the coronary vessel walls more accurately. In comparison to the state-of-the-art methods, our model segments lumen, intima, and media with higher accuracy, higher Dice coefficient, and lower average boundary error values. Simultaneously, our method adds the additional capabilities to analyze thickened vessel walls and detect guidewire and plaque shadows. This

open-source model enables the researchers and physicians to answer biological questions and improve patient care by facilitating rapid downstream image analyses and geometrical characterizations.

TABLE V

ABLATION STUDY OF POST-PROCESSING AND EXCLUSION CRITERIA.

Post-processing	Normal Wall	Thickened Wall	Absolute Distance Error (μm)		
			Outer Lumen	Outer Intima	Outer Media
×	✓	✓	2.60 ± 3.17	30.64 ± 59.73	19.81 ± 27.58
×	✓	×	2.36 ± 3.88	6.89 ± 9.99	7.53 ± 8.64
×	×	✓	2.38 ± 2.04	37.31 ± 67.08	21.35 ± 28.65
✓	✓	✓	2.60 ± 3.18	16.90 ± 24.86	20.85 ± 35.56
✓	✓	×	2.36 ± 3.88	7.02 ± 11.05	7.68 ± 9.23
✓	×	✓	2.38 ± 2.04	17.55 ± 25.92	22.59 ± 37.41

REFERENCES

- [1] S. S. Virani, A. Alonso, E. J. Benjamin, M. S. Bittencourt, C. W. Callaway, A. P. Carson, A. M. Chamberlain, A. R. Chang, S. Cheng, F. N. Delling *et al.*, "Heart disease and stroke statistics—2020 update: a report from the american heart association," *Circulation*, vol. 141, no. 9, pp. e139–e596, 2020.
- [2] M. Franco, R. S. Cooper, U. Bilal, and V. Fuster, "Challenges and opportunities for cardiovascular disease prevention," *The American journal of medicine*, vol. 124, no. 2, pp. 95–102, 2011.
- [3] A. Arbab-Zadeh, M. Nakano, R. Virmani, and V. Fuster, "Acute coronary events," *Circulation*, vol. 125, no. 9, pp. 1147–1156, 2012.
- [4] N. Meneveau, G. Souteyrand, P. Motreff, C. Caussin, N. Amabile, P. Ohlmann, O. Morel, Y. Lefrançois, V. Descotes-Genon, J. Silvain *et al.*, "Optical coherence tomography to optimize results of percutaneous coronary intervention in patients with non–st-elevation acute coronary syndrome: results of the multicenter, randomized doctors study (does optical coherence tomography optimize results of stenting)," *Circulation*, vol. 134, no. 13, pp. 906–917, 2016.
- [5] J. Narula, M. Nakano, R. Virmani, F. D. Kolodgie, R. Petersen, R. Newcomb, S. Malik, V. Fuster, and A. V. Finn, "Histopathologic characteristics of atherosclerotic coronary disease and implications of the findings for the invasive and noninvasive detection of vulnerable plaques," *Journal of the American College of Cardiology*, vol. 61, no. 10, pp. 1041–1051, 2013.
- [6] I.-K. Jang, G. Tearney, and B. Bouma, "Visualization of tissue prolapse between coronary stent struts by optical coherence tomography: comparison with intravascular ultrasound," *Circulation*, vol. 104, no. 22, pp. 2754–2754, 2001.
- [7] T. Okamura, Y. Onuma, H. M. Garcia-Garcia, R. J. van Geuns, J. J. Wykrzykowska, C. Schultz, W. J. Van Der Giessen, J. Ligthart, E. Regar, and P. W. Serruys, "First-in-man evaluation of intravascular optical frequency domain imaging (ofdi) of terumo: a comparison with intravascular ultrasound and quantitative coronary angiography," *EuroIntervention: journal of EuroPCR in collaboration with the Working Group on Interventional Cardiology of the European Society of Cardiology*, vol. 6, no. 9, pp. 1037–1045, 2011.
- [8] M. Pazdernik, H. Bedanova, Z. Chen, J. Kautzner, V. Melenovsky, I. Malek, A. Slavcev, M. Bartonova, V. Karmazin, T. Eckhardt *et al.*, "Donor specific anti-hla antibodies and cardiac allograft vasculopathy: A prospective study using highly automated 3-d optical coherence tomography analysis," *Transplant Immunology*, p. 101340, 2020.
- [9] O. Manfrini, E. Mont, O. Leone, E. Arbustini, V. Eusebi, R. Virmani, and R. Bugiardini, "Sources of error and interpretation of plaque morphology by optical coherence tomography," *The American journal of cardiology*, vol. 98, no. 2, pp. 156–159, 2006.
- [10] S. K. Nadkarni, M. C. Pierce, B. H. Park, J. F. de Boer, P. Whittaker, B. E. Bouma, J. E. Bressner, E. Halpern, S. L. Houser, and G. J. Tearney, "Measurement of collagen and smooth muscle cell content in atherosclerotic plaques using polarization-sensitive optical coherence tomography," *Journal of the American College of Cardiology*, vol. 49, no. 13, pp. 1474–1481, 2007.
- [11] M. Villiger, K. Otsuka, A. Karanasos, P. Doradla, J. Ren, N. Lippok, M. Shishkov, J. Daemen, R. Diletti, R.-J. van Geuns *et al.*, "Coronary plaque microstructure and composition modify optical polarization: a new endogenous contrast mechanism for optical frequency domain imaging," *JACC: Cardiovascular Imaging*, vol. 11, no. 11, pp. 1666–1676, 2018.
- [12] E. M. Tuzcu, S. R. Kapadia, E. Tutar, K. M. Ziada, R. E. Hobbs, P. M. McCarthy, J. B. Young, and S. E. Nissen, "High prevalence of coronary atherosclerosis in asymptomatic teenagers and young adults: evidence from intravascular ultrasound," *Circulation*, vol. 103, no. 22, pp. 2705–2710, 2001.
- [13] G. Litjens, T. Kooi, B. E. Bejnordi, A. A. A. Setio, F. Ciompi, M. Ghafoorian, J. A. Van Der Laak, B. Van Ginneken, and C. I. Sánchez, "A survey on deep learning in medical image analysis," *Medical image analysis*, vol. 42, pp. 60–88, 2017.
- [14] A. Hosny, C. Parmar, J. Quackenbush, L. H. Schwartz, and H. J. Aerts, "Artificial intelligence in radiology," *Nature Reviews Cancer*, vol. 18, no. 8, pp. 500–510, 2018.
- [15] J. De Fauw, J. R. Ledsam, B. Romera-Paredes, S. Nikolov, N. Tomasev, S. Blackwell, H. Askham, X. Glorot, B. O'Donoghue, D. Ventin *et al.*, "Clinically applicable deep learning for diagnosis and referral in retinal disease," *Nature medicine*, vol. 24, no. 9, pp. 1342–1350, 2018.
- [16] A. Abdolmanafi, L. Duong, N. Dahdah, I. R. Adib, and F. Cherié, "Characterization of coronary artery pathological formations from oct imaging using deep learning," *Biomedical Optics Express*, vol. 9, no. 10, pp. 4936–4960, 2018.
- [17] A. Abdolmanafi, N. Dahdah, L. Duong, R. I. Adib, and F. Cherié, "Fully automatic artificial intelligence diagnostic model of coronary artery lesions using oct imaging," *Canadian Journal of Cardiology*, vol. 35, no. 10, pp. S61–S62, 2019.
- [18] M. Henglin, G. Stein, P. V. Hushcha, J. Snoek, A. B. Wiltshcko, and S. Cheng, "Machine learning approaches in cardiovascular imaging," *Circulation: Cardiovascular Imaging*, vol. 10, no. 10, p. e005614, 2017.
- [19] M. C. Moraes, D. A. C. Cardenas, and S. S. Furuie, "Automatic lumen segmentation in ivoct images using binary morphological reconstruction," *Biomedical engineering online*, vol. 12, no. 1, p. 78, 2013.
- [20] M. Bologna, S. Migliori, E. Montin, R. Rampat, G. Dubini, F. Migliavacca, L. Mainardi, and C. Chiastra, "Automatic segmentation of optical coherence tomography pullbacks of coronary arteries treated with bioresorbable vascular scaffolds: Application to hemodynamics modeling," *PLoS one*, vol. 14, no. 3, p. e0213603, 2019.
- [21] M. M. Macedo, W. V. Guimarães, M. Z. Galon, C. K. Takimura, P. A. Lemos, and M. A. Gutierrez, "A bifurcation identifier for iv-oc using orthogonal least squares and supervised machine learning," *Computerized medical imaging and graphics*, vol. 46, pp. 237–248, 2015.
- [22] M. M. G. d. Macedo, C. K. Takimura, P. A. Lemos, and M. A. Gutierrez, "A robust fully automatic lumen segmentation method for in vivo intracoronary optical coherence tomography," *Research on Biomedical Engineering*, vol. 32, no. 1, pp. 35–43, 2016.
- [23] A. Akbar, T. Khwaja, A. Javaid, J.-s. Kim, and J. Ha, "Automated accurate lumen segmentation using l-mode interpolation for three-dimensional intravascular optical coherence tomography," *Biomedical optics express*, vol. 10, no. 10, pp. 5325–5336, 2019.
- [24] G. J. Ughi, T. Adriaenssens, K. Onsea, P. Kayaert, C. Dubois, P. Sinaeve, M. Coosemans, W. Desmet, and J. D'hooge, "Automatic segmentation of in-vivo intra-coronary optical coherence tomography images to assess stent strut apposition and coverage," *The international journal of cardiovascular imaging*, vol. 28, no. 2, pp. 229–241, 2012.
- [25] S. Joseph, A. Adnan, and D. Adlam, "Automatic segmentation of coronary morphology using transmittance-based lumen intensity-enhanced intravascular optical coherence tomography images and applying a localized level-set-based active contour method," *Journal of Medical Imaging*, vol. 3, no. 4, p. 044001, 2016.
- [26] Y. Cao, K. Cheng, X. Qin, Q. Yin, J. Li, R. Zhu, and W. Zhao, "Automatic lumen segmentation in intravascular optical coherence tomography images using level set," *Computational and mathematical methods in medicine*, vol. 2017, 2017.
- [27] A. Wang, J. Eggermont, J. H. Reiber, and J. Dijkstra, "Fully automated side branch detection in intravascular optical coherence tomography pullback runs," *Biomedical optics express*, vol. 5, no. 9, pp. 3160–3173, 2014.
- [28] G. Zahnd, A. Hoogendoorn, N. Combaret, A. Karanasos, E. Péry, L. Sarry, P. Motreff, W. Niessen, E. Regar, G. Van Soest *et al.*, "Contour segmentation of the intima, media, and adventitia layers in intracoronary oct images: application to fully automatic detection of healthy wall regions," *International journal of computer assisted radiology and surgery*, vol. 12, no. 11, pp. 1923–1936, 2017.
- [29] K. Lee, L. Zhang, M. D. Abramoff, and M. Sonka, "Fast and memory-efficient logismos graph search for intraretinal layer segmentation of 3d macular oct scans," in *Medical Imaging 2015: Image Processing*, vol. 9413. International Society for Optics and Photonics, 2015, p. 94133X.
- [30] Z. Chen, M. Pazdernik, H. Zhang, A. Wahle, Z. Guo, H. Bedanova, J. Kautzner, V. Melenovsky, T. Kovarnik, and M. Sonka, "Quantitative 3d analysis of coronary wall morphology in heart transplant patients: Oct-assessed cardiac allograft vasculopathy progression," *Medical image analysis*, vol. 50, pp. 95–105, 2018.
- [31] A. G. Roy, S. Conjeti, S. G. Carlier, P. K. Dutta, A. Kastrati, A. F. Laine, N. Navab, A. Katouzian, and D. Sheet, "Lumen segmentation in intravascular optical coherence tomography using backscattering tracked and initialized random walks," *IEEE journal of biomedical and health informatics*, vol. 20, no. 2, pp. 606–614, 2015.
- [32] S. Tsantis, G. C. Kagadis, K. Katsanos, D. Karnabatidis, G. Bourantas, and G. C. Nikiforidis, "Automatic vessel lumen segmentation and stent strut detection in intravascular optical coherence tomography," *Medical physics*, vol. 39, no. 1, pp. 503–513, 2012.
- [33] M. L. Olender, L. S. Athanasiou, M. José, E. Ben-Assa, F. R. Nezami, and E. R. Edelman, "A mechanical approach for smooth surface fitting to delineate vessel walls in optical coherence tomography images," *IEEE transactions on medical imaging*, vol. 38, no. 6, pp. 1384–1397, 2018.

- [34] S. Yang, H.-J. Yoon, S. J. M. Yazdi, and J.-H. Lee, "A novel automated lumen segmentation and classification algorithm for detection of irregular protrusion after stents deployment," *The International Journal of Medical Robotics and Computer Assisted Surgery*, vol. 16, no. 1, p. e2033, 2020.
- [35] M. Pazdernik, Z. Chen, H. Bedanova, J. Kautzner, V. Melenovsky, V. Karmazin, I. Malek, A. Tomasek, E. Ozabalova, J. Krejci *et al.*, "Early detection of cardiac allograft vasculopathy using highly automated 3-dimensional optical coherence tomography analysis," *The Journal of Heart and Lung Transplantation*, vol. 37, no. 8, pp. 992–1000, 2018.
- [36] Y. L. Yong, L. K. Tan, R. A. McLaughlin, K. H. Chee, and Y. M. Liew, "Linear-regression convolutional neural network for fully automated coronary lumen segmentation in intravascular optical coherence tomography," *Journal of biomedical optics*, vol. 22, no. 12, p. 126005, 2017.
- [37] Y. Gharaibeh, D. S. Prabhu, C. Kolluru, J. Lee, V. Zimin, H. G. Bezerra, and D. L. Wilson, "Coronary calcification segmentation in intravascular oct images using deep learning: application to calcification scoring," *Journal of Medical Imaging*, vol. 6, no. 4, p. 045002, 2019.
- [38] K. Otsuka, M. Villiger, S. K. Nadkarni, and B. E. Bouma, "Intravascular polarimetry for tissue characterization of coronary atherosclerosis," *Circulation reports*, vol. 1, no. 12, pp. 550–557, 2019.
- [39] —, "Intravascular polarimetry: Clinical translation and future applications of catheter-based polarization sensitive optical frequency domain imaging," *Frontiers in Cardiovascular Medicine*, vol. 7, 2020.
- [40] K. Otsuka, M. Villiger, L. J. van Zandvoort, T. Neleman, A. Karanasos, J. Dijkstra, G. van Soest, E. Regar, S. K. Nadkarni, J. Daemen *et al.*, "Polarimetric signatures of vascular tissue response to drug-eluting stent implantation in patients," *Cardiovascular Imaging*, vol. 13, no. 12, pp. 2695–2696, 2020.
- [41] M. Villiger, E. Z. Zhang, S. K. Nadkarni, W.-Y. Oh, B. J. Vakoc, and B. E. Bouma, "Spectral binning for mitigation of polarization mode dispersion artifacts in catheter-based optical frequency domain imaging," *Optics express*, vol. 21, no. 14, pp. 16 353–16 369, 2013.
- [42] O. Ronneberger, P. Fischer, and T. Brox, "U-net: Convolutional networks for biomedical image segmentation," in *International Conference on Medical image computing and computer-assisted intervention*. Springer, 2015, pp. 234–241.
- [43] K. He, X. Zhang, S. Ren, and J. Sun, "Deep residual learning for image recognition," in *Proceedings of the IEEE conference on computer vision and pattern recognition*, 2016, pp. 770–778.
- [44] F. Milletari, N. Navab, and S.-A. Ahmadi, "V-net: Fully convolutional neural networks for volumetric medical image segmentation," in *2016 fourth international conference on 3D vision (3DV)*. IEEE, 2016, pp. 565–571.
- [45] M. Arjovsky, S. Chintala, and L. Bottou, "Wasserstein gan," *arXiv preprint arXiv:1701.07875*, 2017.
- [46] C. Villani, *Optimal transport: old and new*. Springer Science & Business Media, 2008, vol. 338.
- [47] I. Gulrajani, F. Ahmed, M. Arjovsky, V. Dumoulin, and A. C. Courville, "Improved training of wasserstein gans," in *Advances in neural information processing systems*, 2017, pp. 5767–5777.
- [48] M.-P. Dubuisson and A. K. Jain, "A modified hausdorff distance for object matching," in *Proceedings of 12th international conference on pattern recognition*, vol. 1. IEEE, 1994, pp. 566–568.
- [49] M. Villiger, K. Otsuka, A. Karanasos, P. Doradla, J. Ren, N. Lippok, M. Shishkov, J. Daemen, R. Diletti, R.-J. van Geuns *et al.*, "Repeatability assessment of intravascular polarimetry in patients," *IEEE transactions on medical imaging*, vol. 37, no. 7, pp. 1618–1625, 2018.
- [50] K.-P. Tung, W.-Z. Shi, R. De Silva, E. Edwards, and D. Rueckert, "Automatic vessel wall detection in intravascular coronary oct," in *2011 IEEE International Symposium on Biomedical Imaging: From Nano to Macro*. IEEE, 2011, pp. 610–613.
- [51] Z. Wang, H. Kyono, H. G. Bezerra, D. L. Wilson, M. A. Costa, and A. M. Rollins, "Automatic segmentation of intravascular optical coherence tomography images for facilitating quantitative diagnosis of atherosclerosis," in *Optical Coherence Tomography and Coherence Domain Optical Methods in Biomedicine XV*, vol. 7889. International Society for Optics and Photonics, 2011, p. 78890N.
- [52] G.-A. Cheimariotis, Y. S. Chatzizisis, V. G. Koutkias, K. Toutouzas, A. Giannopoulos, M. Riga, I. Chouvarda, A. P. Antoniadis, C. Doulavarakis, I. Tsamboulatidis *et al.*, "Arcoct: Automatic detection of lumen border in intravascular oct images," *Computer Methods and Programs in Biomedicine*, vol. 151, pp. 21–32, 2017.
- [53] M. L. Olender, L. S. Athanasiou, M. José, E. Ben-Assa, and E. R. Edelman, "Simultaneous multi-surface fitting for vessel wall layer delineation," in *2019 IEEE EMBS International Conference on Biomedical & Health Informatics (BHI)*. IEEE, 2019, pp. 1–4.
- [54] Q. Xiong, N. Wang, X. Liu, S. Chen, C. S. Braganza, B. E. Bouma, L. Liu, and M. Villiger, "Constrained polarization evolution simplifies depth-resolved retardation measurements with polarization-sensitive optical coherence tomography," *Biomedical Optics Express*, vol. 10, no. 10, pp. 5207–5222, 2019.